Optics & Laser Technology 149 (2022) 107916

Contents lists available at ScienceDirect

Optics and Laser Technology

journal homepage: www.elsevier.com/locate/optlastec

Dynamically control selective photo response in the visible light using phase change material

Bowei Zhang [a], Yaxiong Tao [a], Sandeep Kumar Chamoli [b,*], Qi Chen [c], Kuo Zhao [a], YueHua Yu [a], Bin Wang [a]

[a] Chongqing College of Electronic Engineering (CQCEE), Chongqing 401331, China
[b] Changchun Institute of Optics, Fine Mechanics and Physics, Chinese Academy of Sciences, China
[c] College of Optoelectronic Engineering, Changchun University of Science and Technology, Changchun, Jilin 130022, China

A B S T R A C T

A photodetector with a selective wavelength response is essential for many applications such as imaging, machine vision, and colour identification in particular. A state-of-the-art wavelength selective photodetector is a broadband photodetector mounted with a dichroic prism or an optical filter for selectivity. Furthermore, some of the designs depend on the engineering of the ratio of active material, for example, in triple halide lead perovskite for selective response. Here we numerically propose selective photoresponse using phase-change-material (PCM) antimony trisulfide (Sb_2S_3) as an active medium. Sb_2S_3 shows fast ~70 ns and reversible phase transition between its Crystalline (Cry) and Amorphous (Amp) phase with significant contrast in refractive index. The phase transition can be controlled dynamically either by tharmal or optical means. The photo response (R) is optimized for 552 nm (green light) and 691 nm (red light) with R ~0.5 A/W and R ~0.6 A/W respectively. Moreover, we have shown that by integrating radiative cooling approach one can manage the heat accumulation due to photocurrent or incident light to maintain it's damage threshold. We have realized that one can maintain the PD temperature near to the ambience temperature even at 1000 W/m^2. According to the simulations, the calculated operating temperatures under 1000 W/m^2 with and without radiative cooling are respectively 305 K and 345 K.

1. Introduction

Photo detectors (PDs) have great importance in many applications such as imaging, telecommunication, bio sensing, and environment surveillance [1–5]. Based on their spectral response window, PDs are divided into two main categories namely broadband [6–12] and narrowband PDs [13]. PDs with broadband response always have high external quantum efficiency (EQE) and are broadly used under low light conditions for multi-colour photo detection [14–16]. On the other hand, narrowband photodetector is extremely useful where colour discrimination is essential. This can be achieved by combining either dichroic prism (DP) or optical filter (OF) at the input of broadband PD [17–19]. DP is a widely used strategy for narrowband response but it makes the system complicated and degrades the image quality. There has been remarkable progress to investigate a new material combination for PD which can selectively detect the wavelength of interest with high EQE [4]. It is possible to achieve the narrow full width at half maxim (FWHM) using organic photodiodes (OPDs), but suppression outside the wavelength of interest remains the challenge [18]. Red light (620–750 nm) PDs are suitable for short-distance optical communication and also have an important role to play in three- and four-color photo sensors. Near infrared (NIR) detects are very useful in medical, industries, communications, scientific and military including night vision imaging and security.

Many strategies and material combinations have been adopted to achieve the PD with selective narrowband response such as using organic narrowband absorber in the photodiode active layer [20], controlling the absorption of light in active layer [18], concept of charge collection narrowing (CCN) using organohalide perovskite and lead halide perovskite and organic semiconductor [21,22]. CCN method is used for manipulation of internal quantum efficiency (IQE) of PD. In this method the device is manipulated such that only volume generated charges (appearing at incident light energy near optical gap energy of junction materials) gets collected and contribute to the current. A selective response in the red, green and blue region with FWHM of 100 nm has been shown using organohalide perovskite and lead halide perovskite and tunability was achieved by varying the ratio halide [21]. Rare-earth elements, such as In and Te, are in limited supply on earth, and Cd and Pb are toxic. This creates a crucial need of photovoltaic absorber material which is natural on earth, nontoxic, cost-effective and scalable in process. Sb_2S_3 is a fascinating photovoltaic (PV) material due to its earth-abundant, nontoxic components and a high absorption coefficient

* Corresponding author.
E-mail address: boevyzbw@163.com (S.K. Chamoli).

https://doi.org/10.1016/j.optlastec.2022.107916
Received 18 November 2021; Received in revised form 10 January 2022; Accepted 25 January 2022
Available online 2 February 2022

($\alpha > 10^4$ cm^{-1}). It is a binary compound with a single stable phase and therefore devoid of the risk of forming unfavourable secondary phases. Furthermore, because of low Sb_2S_3's melting point (550 °C), high crystalline quality films can be synthesized at low temperatures (350 °C). The values of ϕ_b (at Au/Sb_2S_3) and Eg in Cry and Amp phases in Sb_2S_3 are (1 eV, 1.72 eV) and (0.35 eV, 2.01 eV) respectively. Due to this, Sb_2S_3 has recently emerged as a promising candidate because of its unique properties, including: high band gap, high absorption coefficient, and environment friendly and huge availability on earth for many applications such as optical modulator and hot electron photodetector [23,24]. Additionally, exploiting the ability to undergo rapid, reversible changes between two or more stable phases that possess different optoelectronic properties [25,26]. A wide variety of thin film and nanowire based Sb_2S_3 applications are being investigated, including solar cells [27], water splitting [28], photodetection [29–34], and tunable photonics applications [35,36]. A number of new fabrication methods are also being explored. However, due to the diffusion issue between Sb_2S_3 and noble metal fabrication is still a challenging task. To solve the diffusion problem a 5 nm thick Si_3N_4 layer was introduced between metal and Sb_2S_3 as shown in the reference [37]. Sb_2S_3 can switch its phase from crystalline to amorphous optically, using an ultrafast pulsed laser, [9] or thermally, e.g., using ITO or graphene micro heaters below the phase change material [38,39]. Phase transition in Sb_2S_3 from Cry to Amp or Amp to Cry phase takes place in 70 ns resulting in ~7.14 MHz of switching speed or modulation frequency [37].

In this paper, we have numerically proposed an efficient strategy to achieve dynamic control on narrowband photo response in the visible range due to significant index contrast present in the Sb_2S_3. A dielectric mirror (DM) made of TiO_2/MgF_2 employed to achieve sharp narrowband photo response on the top of Sb_2S_3. Combining DM and Sb_2S_3 with its phase change nature selective narrow response with FWHM < 100 nm has been achieved. Hyperbolic metamaterial (HMM) made of 3 bilayers of silicon dioxide (SiO_2) and gold (Au), used as a substrate and significantly increases the quality factor (Q- factor) of resonance. It shows a nature of Type I HMM, where the uniaxial anisotropic permittivity values are such $\varepsilon\| = \varepsilon_x = \varepsilon_y > 0$ and $\varepsilon_\perp = \varepsilon_z < 0$ where $\varepsilon\|$ and $\varepsilon_\perp$ are parallel and perpendicular permittivity, respectively and ε_x, ε_y and ε_z are effective permittivity in the ×, y and z directions, respectively. The frequency at which $\varepsilon\| \times \varepsilon_\perp < 0$ corresponds to a topological transition from elliptical to hyperbolic dispersion can be conveniently calculated using the effective medium theory. The perpendicular and parallel permittivity of the system are given by [40–42].

$$\varepsilon\| = f_m\varepsilon_m + f_d\varepsilon_d \tag{1}$$

$$\varepsilon_\perp = \frac{\varepsilon_m\varepsilon_d}{f_m\varepsilon_m + f_d\varepsilon_d} \tag{2}$$

where ε_d and ε_m are the complex permittivity of metal and dielectric respectively, f_m and f_d are the fill fraction of metal and dielectric in the structure and can be calculated as follows: $f_m = \frac{t_m}{t_m + t_d}$ and $f_d = 1 - f_m$, where t_m and t_d are the layer thicknesses of metal and dielectric in a unit cell. So basically, HMM behaves like a dielectric (positive permittivity) below the transition wavelength and metal (negative permittivity) above transition wavelength (~500 nm). That helps to have resonance in the targeted wavelength of 552 nm and 691 nm.

2. Result and discussion

The schematic of proposed PD is shown in Fig. 1 (a) and (b). It's a combination of DM and PCM on HMM substrate. DM is a combination of 50 nm titanium dioxide (TiO_2) and 50 nm magnesium difluoride (MgF_2) followed by Sb_2S_3 as an active medium. Substrate is HMM consists of 3 bilayers of SiO_2 and gold (Au). The Sb_2S_3 thickness has been optimized for high response at ~552 nm and ~691 nm in Amp and Cry phase respectively. The critical light coupling into the cavity is given by: $2nh = (m + 1/2)\,\lambda_0$, where n is the refractive index of cavity (Sb_2S_3), m

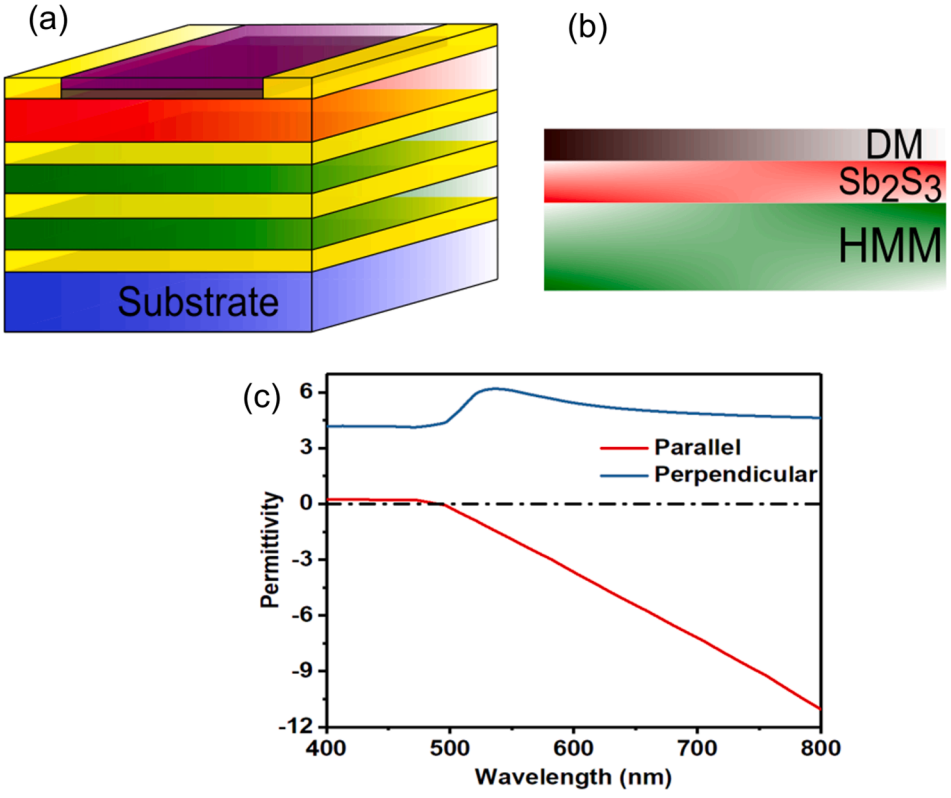

Fig. 1. Schematic of proposed PD (a) 3 –D (b) 2-D. DM consists of 50 nm TiO_2 and MgF_2, Sb_2S_3 is 110 nm thick. HMM is made of 3 bilayers of Au (5 nm)/SiO_2 (10 nm). (c) perpendicular ($\boldsymbol{\varepsilon}_\perp$) and parallel ($\boldsymbol{\varepsilon}\|$) permittivity for HMM.

represents mode order, λ_0 represents resonance wavelength and h is the Sb_2S_3 thickness. In terms of modes supported by the cavities, the number of modes can be increased or decreased significantly by adjusting h. Typically, supported modes follow a resonance condition. Optimized h is 110 nm. Au electrodes are in direct contact with Sb_2S_3 and DM. Au has been chosen due to having lowest Schottky barrier height (ϕ_b) with Sb_2S_3 and better stability than other metals such as Al and Ag. There is a noticeable difference in index and absorption coefficient between the Cry and Amp phases of Sb_2S_3 with nanosecond switching speed ~70 ns, large band gap and low losses, which contributes to its ability to be used in both visible and NIR photonic applications [14]. A transfer matrix method (TMM) is used in FDTD lumerical to simulate optical systems. From 400 to 800 nm, light penetrates the structure in the downward Z - direction. The reflectance index for Sb_2S_3 was calculated using the following reference [37].

Fig. 2 (a) and (b) show contrast in absorption coefficient and index (Δn & Δk) for Cry and Amp phase of Sb_2S_3 depending on the wavelength of the incident light. Amp Sb_2S_3 exhibits a higher refractive index than Cry, with the maximum difference reaching $\Delta n \sim 1$ Δn 1 at 614 nm. Cry phase imaginary part is negligible after 700 nm, and zero for the Amp phase above 550 nm. This significant difference in index or absorption coefficient of Sb_2S_3 allows for dynamic tuning of the proposed PD. Phase transition in Sb_2S_3 can be tuned by optically or thermally [37]. Fig. 2 (c) and (d) show absorption response of PD with and without mirror. Cry Sb_2S_3 is slightly more absorbing than the Amp state, and this causes a broader resonance in case Cry Sb_2S_3 (see Fig. 2 (c)). It is somewhat revealing that the density of Sb_2S_3 increases from 3.42 ± 0.06 to 4.64 ± 0.06 gcm^{-3} upon crystallization, which corresponds to a 35% increase in density [37,43]. Below bandgap refractive index also increases by 33%. The role of DM is clear *i.e.*, it reflects the light selectively depending upon thickness and significantly increases the Q- factor (narrow line width). DM strongly reflects the light in a region where Sb_2S_3 has strong absorption and provides desired narrow response in a selective wavelength window. Further enhancement in the Q-factor has been observed using HMM as a substrate. The results are optimized for 552 nm (green light) and 691 nm (red light), optimized parameters are (i) DM (MgF_2 + TiO_2) thickness 100 nm, (ii) Sb_2S_3 thickness 110 nm and (c) HHM (Au + SiO_2) unit cell thickness 10 nm.

The cavity can change its absorption band from 400 nm to 800 nm by properly selecting parameters from the resonance condition. Besides h, the resonance condition is also greatly influenced by the cavity (Sb_2S_3) index n and can be dynamically controlled use to Sb_2S_3. The electric field distribution of the proposed Amp and Cry PD are shown in Fig. 3 (a) and (b), respectively. We have calculated the field distribution versus wavelength and propagation direction (Z). As shown in Amp phase, the DM confines light before 550 nm while selectively allowing light at 552 nm to pass. In contrast, after the phase transition to Cry phase, light beyond 700 nm is allowed to pass the DM. With narrow bands and high enhancements at resonance wavelengths, the electromagnetic field is mainly distributed in the middle layer (Sb_2S_3). There are two easy-to-see distribution windows: (i) A window <550 nm and 700 nm in Amp and Cry phase, which is following a Beer Lambert region (B. L. region) (ii) After 550 nm and 750 nm interference regions in which the absorbing media (Sb_2S_3) can be completely penetrated and then reflected back from the bottom HMM substrate (Interference region). Due to constructive interference between incoming and reflected light from the HMM in the interference region, the electric field at resonance becomes highly confined to the Sb_2S_3 layer or after B. L. region. In the B. L. region, the photo generated electrons reside on the surface of DM and Sb_2S_3 and known as 'surface generation'. However, in the cavity region carriers are generated throughout the junction region including bottom Au layer and known as 'volume generation'. It is also important to note for thin Sb_2S_3 all the incident light can create volume charge with decent efficiency due to short extraction length for both the e^- and hole and ultimately shows broad EQE response. However, increasing Sb_2S_3 thickness increases surface charge in B.L. region and selective spectral response in interference region can be seen and used as PD for colour discrimination. Furthermore, the electric field intensity profile at 552 nm and 691 nm has been shown in Fig. 3 (c) for Amp and Cry.

The EQE of proposed PD has been calculated following [44] and verified with this work [21,22]. EQE is always low for surface generated regions due to high recombination probability because of bulky local

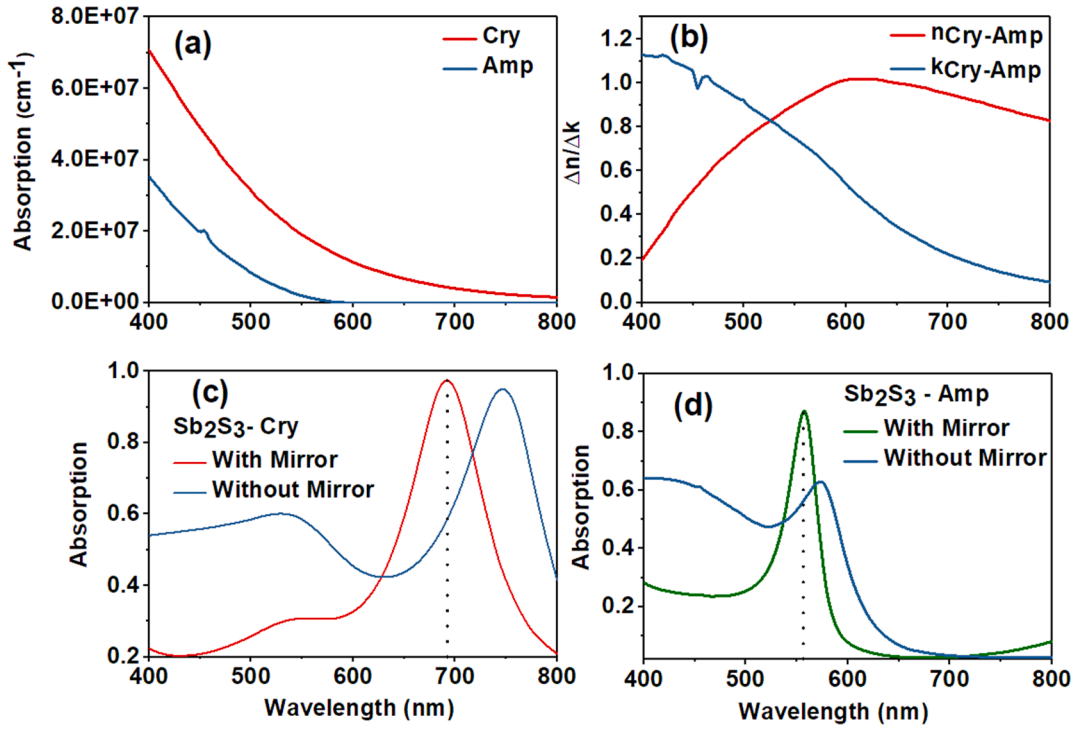

Fig. 2. (a) Absorption coefficient (b) Wavelength-dependent contrast in the Cry and Amp phases. PD Absorption with and without mirror in for (c) Sb_2S_3 in Cry and (d) Sb_2S_3 in Amp.

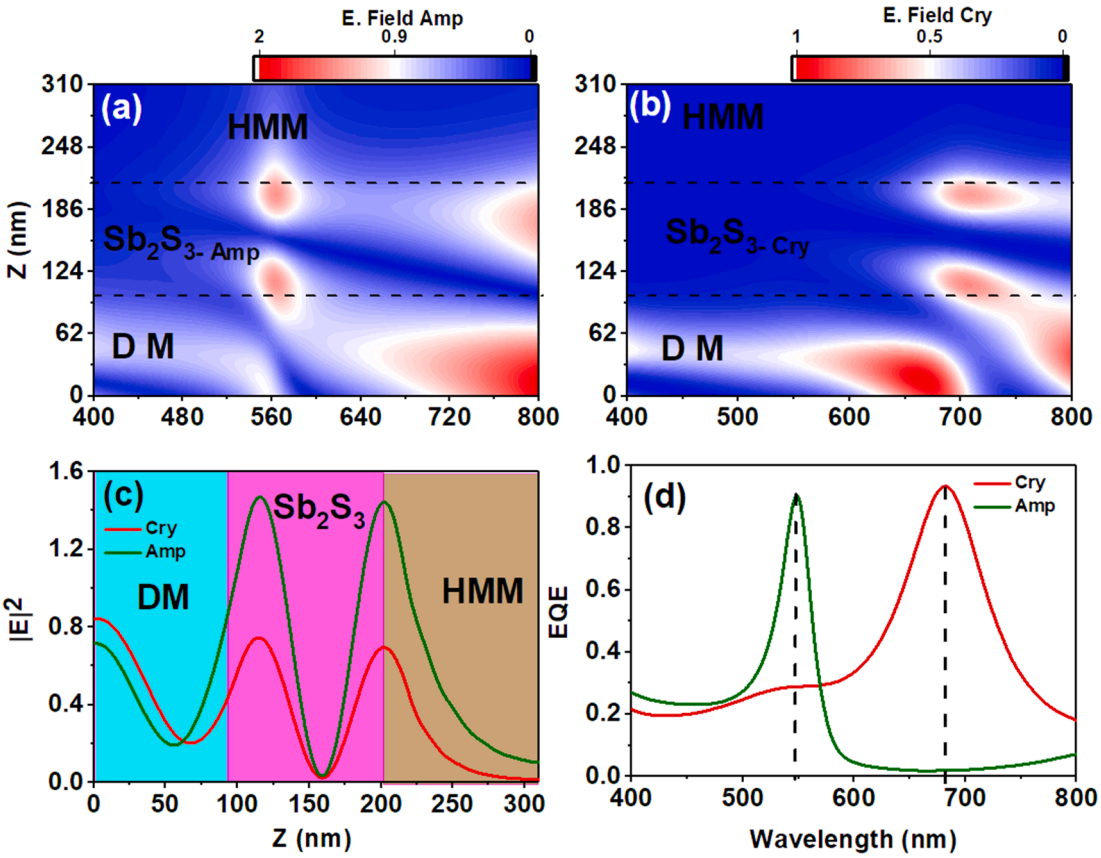

Fig. 3. Wavelength and location of the electromagnetic field in the device (a) Amp phase, (b) Cry phase (c) Electric field intensity in Cry and Amp phase at wavelength of 815 nm and 550 nm, respectively depending on the device's location (d) EQE in Cry and Amp phase responding in red and NIR region.

carrier concentration and also transit time imbalance of e^- and holes [22]. On the other hand, in volume generated region recombination probability is low and selectively high EQE. In Fig. 3 (d), the B. L. region shows almost the same i.e., a flat EQE response however in the interference region strong enhancement can be seen corresponding to a particular wavelength. The calculated maximum EQE in Amp and Cry phase are ~90 % at 552 nm (green light) and 691 nm (red light) respectively. The EQE is basically a product of following four efficiencies: (i) photon absorption that leads to exciton generation η_A, (ii) exciton diffusion η_{ED}, (iii) charge dissociation η_{CT}, and (iv) collection of free charges via electrodes η_{CC}. Including all the four factors expression for EQE is given by following formula:

$$\eta_{EQE} = \eta_A \eta_{ED} \eta_{CT} \eta_{CC} \tag{3}$$

η_{ED} is the probability of an electron to reach the junction before recombination. The e^- diffusion length is the length that e^- can travel without being recombined so it is very important to consider in photovoltaic. Therefore, high e^- diffusion length can enhance the charge collection and light harvesting efficiency, which can improve the performance of devices. The e^- diffusion length for Sb_2S_3 is 300 nm, which is greater than the active layer (Sb_2S_3) thickness and can certainly increase the change transport as well as collection. We have considered η_{CT} and η_{CC} ~ 100 %, following the same approach given in [44]. Term $\eta_A \eta_{ED}$ depends on material properties, excitation wavelength, thickness of the layers and its configuration. It can be estimated by calculating electric field intensity in each layer of device.

To predict the electrical performance of proposed heterostructure Current (I) - Voltage (V) analysis is carried out. The I-V relation is given by:

$$I = AA^*T2exp(-q\Phi_b/kT)[\exp(\mathrm{eV/kT}) - 1] \tag{4}$$

where $A = 0.2\ \mathrm{cm}^2$ is the effective area of PD, $I_d = AA^*T^2exp\,(-q\Phi_b/kT)$, $A^* = 4\pi qmek^2/h^3$ Indicates Richardson constant, q represents elementary charge, k Shows Boltzmann constant, h displays Planck constant and m_e is the effective mass (m_e ~1.035 m_0 for Sb_2S_3, m_0 is e^- mass in free space). A^* value is ~125 A/ (cm^2/K^2) for Sb_2S_3 at room temperature (300 K). Upon illumination the number of generated change carriers are given by photocurrent $I_{opt} = \eta I_0 A q \lambda / hc$ modified diode Eq. (4):

$$I = AA^*T2exp(-q\Phi_b/kT)[exp(eV/kT) - 1] - \eta I0Aq\lambda/hc \tag{5}$$

I_0 is the irradiance (illumination intensity) of incident laser light. Fig. 4 (a) shows the I-V curve at 550 nm and 800 nm in Amp and Cry phase respectively with an irradiance of 500 Wm^{-2} falling on the active area of PD. Moreover, the figure of merit (FOM) for any detector depends on its photoresponsivity (R) and detectivity (D). Photoresponsivity is the ability of PD to respond to the incident light and given by the ratio of current generated to power of incident light.

$$R = \frac{\boldsymbol{I_{opt}} - \boldsymbol{I_{dark}}}{\boldsymbol{I_0}} \tag{6}$$

I_{dark} is the current without illumination at a certain applied voltage. Detectivity is also a critical parameter to characterize the ability of PD to detect the low optical signal and given by following expression:

$$D = \frac{\boldsymbol{R}.\sqrt{\boldsymbol{A}}}{\sqrt{2e\boldsymbol{I}_{dark}}} \tag{7}$$

Estimated D and R as a function of incident light with irradiance of 200 Wm^{-2} at $V = 0.2$ V are shown in Fig. 4 (c) and (d) respectively. The I-V curve has been simulated for green and red light with irradiance of 500 Wm^{-2} in Amp and Cry phase, respectively. We can observe similar fill factors (FFs) in both the cases with a difference in short circuit

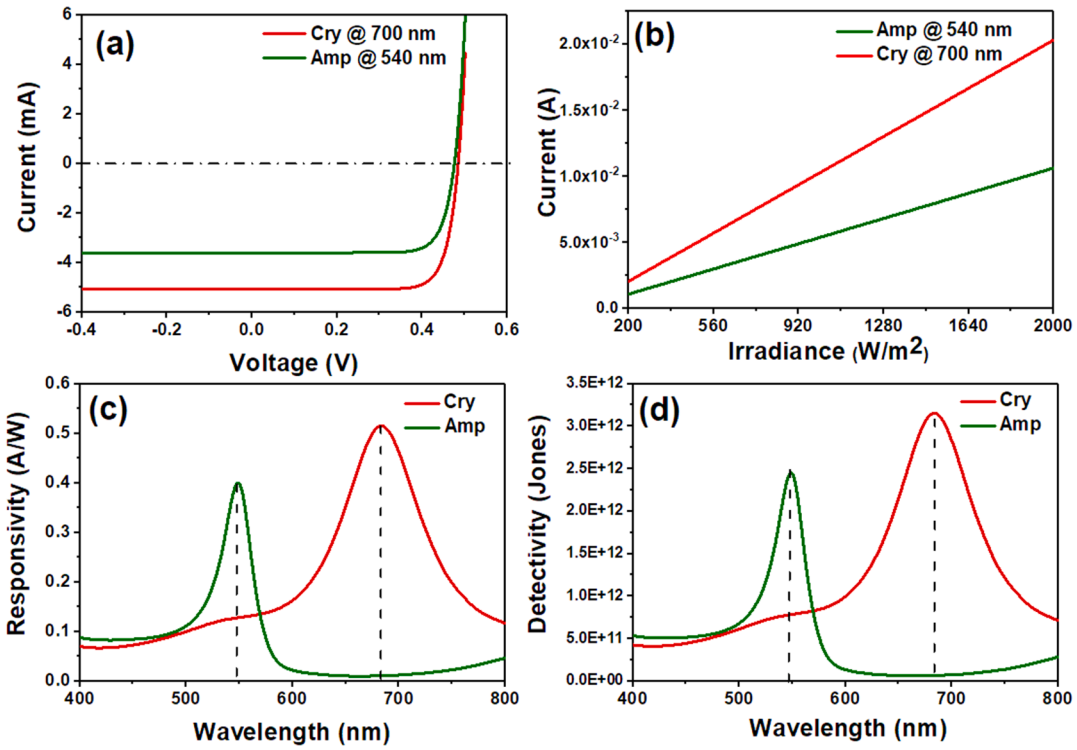

Fig. 4. (a) Current-voltage measurement at 800 nm and 550 nm @ 500 W/m^2 (b) Current with varying irradiance at 800 nm and 550 nm at V = 0 V, (c) detectivity as a function of wavelength at V = 0.2 V and (d) Responsivity as a function of wavelength V = 0.2 V, detector area 0.2 cm^2.

current for 540 nm and 700 nm. Similar FF shows that transport performance of long-lived carriers is preserved and sudden change in short circuit current has a high rate of recombination or low generation rate [11]. Furthermore, we also investigate the current variation as a function of irradiance (intensity dependent photocurrent) at 550 nm in Amp phase and 800 nm in Cry phase (see Fig. 4 (b)). The responsivity and detectivity at 550 nm and 800 nm are maximum in Amp and Cry phase, respectively as shown in the Table 1. Our dark current calculations and detectability values are comparable to the experimentally proposed values for thin film based Sb_2S_3 PD [45]. We have also drawn a comparison Table 2 at the end comparing the responsivity and detectivity of our detector with previous detectors.

2.1. Radiative cooling for photodetector

Generally, photocurrent and light incident on the PD active area generate heat in the PD. The total heating power is equal to the power absorbed from incident light and photocurrent times the voltage applied to the PD. In higher bias voltages, the heating effect due to photocurrent dominates the heating caused by light absorption, limiting the device's operating bias voltage. This limitation may result in damage to the PD semiconductor chip or even a loss of soldering connections. Hence, PD requires an effective heat management method. Here we integrate passive cooling by radiating heat outward [46–48]. Radiative cooling can manage its heat by releasing thermal radiation to outer space in conjunction with a transparency window of 8–13 μm associated with blackbody peak at 300 K. The terrestrial body can therefore manage its heat by releasing thermal radiation to outer space. Fig. 5 illustrates the proposed PD with cooler. SiO_2 and Si_3N_4 are commonly used materials for radiative cooling due to their high emissivity in the atmospheric window and negligible absorption in the visible. In addition to serving as a DM, the top two 200 nm thick layers (SiO_2 + Si_3N_4) also contribute to cooling. Fig. 6 shows the total emissivity/absorptivity of the proposed device, which shows typical PD response with maximum at 532 nm in the visible and high emissivity within the atmospheric window (yellow shaded region in the inset). Hence, the upper two layers of SiO_2 and Si_3N_4 also act as DM. For radiative cooling, we have computed the overall cooling from the device using FDTD-lumerical and Finite Element Method (FEM) approaches in COMSOL (heat transfer module for radiative cooling). The simulation has been carried out considering ambient temperature of 300 K, absolute pressure 1 Pa and relative humidity ~0. The emissivity/absorptivity of the structure is shown in Fig. 6 from visible to atmospheric transparent window (yellow shaded

Table 1
R, D and I_{Short} at 550 (green light) nm and 800 nm (red light). I_0 = 500 Wm^{-2}.

	R (A/W) @ V = 0.2 V	D (Jones) @ V = 0.2 V	I_{short} (mA) @ V = 0 V
540 nm	0.4	2.3 × 10^{12}	−3.6
700 nm	0.52	3 × 10^{12}	−5

Table 2
Comparative table of various photodetectors.

Device	R	D (Jones)	Dynamically control	Ref.
Gr/PdSe2/Ge	691 mA/W	1.73 × 10^{13}	No	[10]
graphene/PtSe2/β-Ga2O3	76.2 mA/W	10^{13}	No	[7]
PdSe2/Si structure	300.2 mA/W	10^{13}	No	[13]
PdSe2/perovskite	313 mA/W	10^{13}	No	[11]
Sb2S3 nanowires	1152 A/W	2 × 10^{13}	No	[30]
Au-nanoparticles- Sb2S3 nanowires	59.5 A/W	4.29 × 10^{10}	No	[33]
RGO–MoS2/pyramid Si	21.8 A/W	3.8 × 10^{15}	No	[12]
Au/Sb2S3/Au devices	0.24 A/W	10^{13}	No	[45]
DM-Sb_2S_3-HMM	0.5 A/W	10^{13}	Yes	This Work

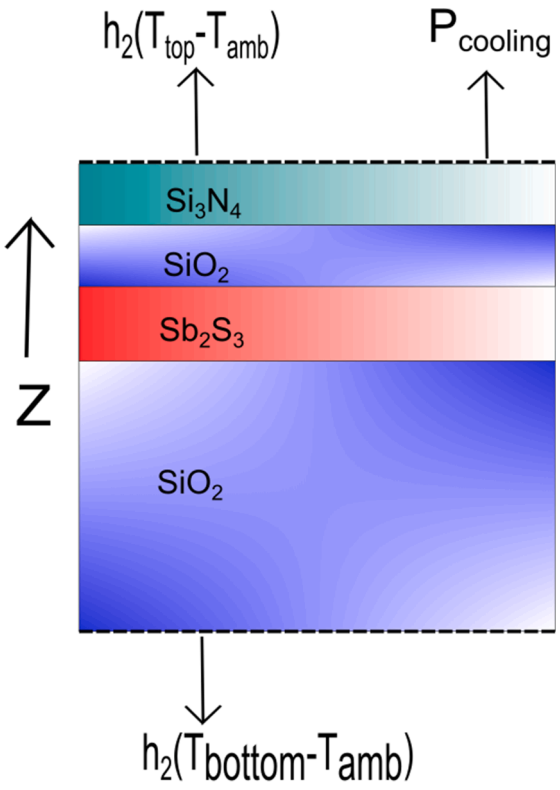

Fig. 5. Schematics of proposed photodetector with cooler, it consists of Si_3N_4 (100 nm) – SiO_2 (100 nm)- Sb_2S_3 (110 nm)– SiO_2 (2000 nm). Si_3N_4-SiO_2 works as a DM and cooler.

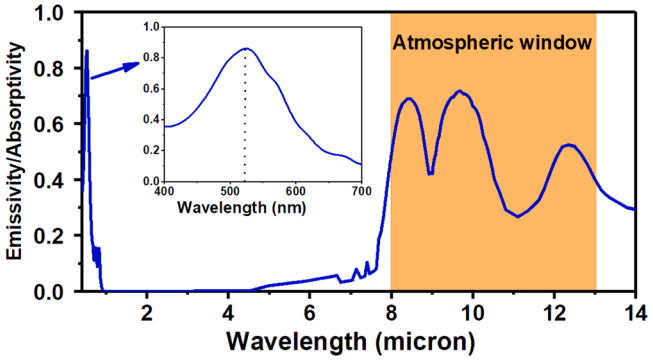

Fig. 6. Emissivity/absorptivity of proposed PD with cooling , yellow highlight (8–13 μm) is atmospheric transmission window.

region in inset).

€Using emissivity results we can further calculate the cooling power of structure by using following expressions [49]:

$$P_{cooling}(T_{Emit}) = P_{rad}(T_{Emit}) - P_{atm}(T_{amb}) \tag{8}$$

where P_{rad} is the power radiated by the structure. T_{Emit} is the temperature at the top surface and will be taken as a boundary temperature in the thermal simulation.

$$Prad(TEmit) = \int d\Omega cos\theta \int_0^\infty d\lambda I_{BB}(T_{Emit}, \lambda)\varepsilon(\lambda, \Omega) \tag{9}$$

$\int d\Omega$ represnts solid angle integrated over a hemisphere and I_{BB} represents blackbody spectral radiance at temperature T. P_{atm} is power absorbed in the ambient atmosphere and expressed as follows:

$$Patm(Tatm) = \int d\Omega cos\theta \int_0^\infty d\lambda I_{BB}(T_{amb}, \lambda)\varepsilon(\lambda, \Omega)\varepsilon_{atm}(\lambda, \Omega) \tag{10}$$

$\varepsilon_{atm}(\lambda, \Omega)$ is the angle dependent emissivity of atmosphere and given by$\varepsilon_{atm}(\lambda, \Omega) = 1 - t\ (\lambda)\ 1/\cos\Theta$, $t(\lambda)$ is atmospheric transmission in the zenith direction. Emissivity results from optical simulation further used in the thermal simulation. Temperature dependent heat capacity and thermal conductivity data for Sb_2S_3 extracted from following reference [19]. The aim is to maintain the selective absorption in visible light using DM and high emissivity in the atmospheric transmission window for radiative cooling. This way we can maintain the PD at low temperature even in case of high incidence power or high operating voltage. The temperature field follows heat diffusion equations:

$$\nabla.(k.\nabla T) + G(r,t) = \rho c_p \partial T/\partial t \tag{11}$$

where t and r are the time and position vector, G (r, t) is energy generation rate. ρandc_p are the density and specific heat capacity at constant pressure of the material. For steady – state case and 1-D simulation heat diffusion Eq. (9) takes the following form:

$$\frac{d}{dz}\left[k(z)\frac{dT(z)}{dz}\right] + G(z) = 0 \tag{12}$$

$k(z)$ is the spatial dependent thermal conductivity of material. Now Eq. (11) can be solved for spatial distribution of temperature in the device by choosing appropriate boundary conditions at the top and bottom surface of PD as shown in schematics. Generally, three boundary conditions one can use: (1) Dirichlet boundary condition for the surface at fixed temperature, (2) Neumann condition corresponds to fixed heat flux, (3) convective boundary condition comes from Newton's law of cooling and (4) radiation boundary condition. Boundary conditions in our case are third at bottom surface (see Eq. (13)) and fourth at the top surface (see Eq. (14)) as shown in schematics.

$$-k(z)\frac{dT(z)}{dz} = h(Tbottom - Tambience) \tag{13}$$

where h is convective heat transfer coefficient and $T_{ambience}$ is the temperature of ambience or surrounding medium. Eq. (13) talks about heat transfer between the bottom surface and its surrounding (in our case it's air). Once the temperature of the device is above absolute zero it emits radiation to the outer surrounding radiatively and is called thermal radiation.

$$-k(z)\frac{dT(z)}{dz} = Prad(Ttop) - Patm(Tatm) + h(Ttop - Tambience) \tag{14}$$

which takes into consideration both the cooling effect due to radiation and non radiative heat loss due to convection. Applying B. C. and Combining FDTD optical simulation with FEM heat diffusion equation, Fig. 7 shows the temperature variation as a function of solar heating power with or without a cooler. The temperature field profile further verifies in MATLAB using self-written numerical code following FEM. It is clear that without the cooler temperature rise from 310 K to 340 K corresponds to 300 W/m^2 to 1000 W/m^2, respectively. On the other hand, and with cooler temperature rise is negligible and at 1000 W/m^2 its rise ~5 K. Fig. 7 inset shows the 2-D temperature profile at 500 W/m^2 with and without cooler. By seeing the significant advantage of radiative cooling approach in controlling operating temperature of PD, one can certainly increase the responsivity of PD at higher operating temperature, where generally device performance degrades due to high temperature.

3. Conclusions

In summary, we have numerically demonstrated a wavelength

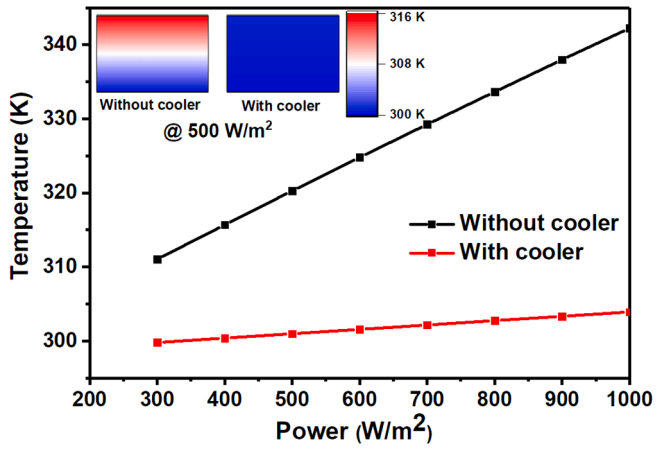

Fig. 7. Temperature variation as a function of solar heating power with or without cooler.

selective PD response using a PCM. In Sb_2S_3 the phase transition from Amp to Cry or Cry to Amp allows for dynamic control of photo response PD. DM reflects the light just before the absorption cutoff, allowing for selective absorption. EQE response shows two distinct region one with broad response efficiency in B. L. region and another one with narrow response in the interference region. In case of Amp Sb2S3, maximum efficiency is at 552 nm (green light), and in case of Cry Sb2S3, maximum efficiency is at 691 nm (red light). The estimated maximum photo-responsivity is 0.4 A/W and 0.52 A/W in the Amp and Cry phase at 552 and 800 nm respectively. The estimated J_d and D values in Amp and Cry phase at 0.2 V are: (4.21×10^{-8} A, 2.2×10^{12} jones @ 552 nm) and (4.33×10^{-8} A and 3.3×10^{12} jones @ 691 nm), respectively. Finally, we presented an integrated approach that incorporated radiative cooling to manage PD temperatures significantly. Apart from being low-cost and dynamically controllable, the proposed PD does not require lithography. Additionally, it can be used for other applications, such as sensing, filtering, and solar applications.

4. Simulation methods

The optical simulations and electric field distribution calculations were conducted using the transfer matrix method in FDTD Lumericals. Using optical response of the device current – voltage equation has been simulated with MATLAB. The final step was to perform a radiative cooling analysis using COMSOL Multiphysics with a heat transfer module and surface to ambient radiation. COMSOL allows users to model or import data for emissivity, device, and atmosphere. In the Radiative Cooling section, each boundary condition is discussed in detail.

Funding

The work is Supported by Research on OAM-MIMO multiplex transmission calibration based on vortex beam project of science and technology research program of Chongqing Education Commission of China (No. KJQN202103102). Also Supported by Research on Multi-Objective Scientific Workflow Scheduling Algorithm in Hybrid Cloud Environment project of science and technology research program of Chongqing Education Commission of China (No. KJQN202003104).

Data availability statement

The data generated and/or analysed during the current study are not publicly available for legal/ethical reasons but are available from the corresponding author on reasonable request.

CRediT authorship contribution statement

Bowei Zhang: Conceptualization, Methodology, Investigation, Data curation, Funding acquisition. **Yaxiong Tao:** Writing – review & editing. **Sandeep Kumar Chamoli:** Conceptualization. **Qi Chen:** Investigation. **Kuo Zhao:** Resources. **YueHua Yu:** Project administration. **Bin Wang:** Funding acquisition, Project administration.

Declaration of Competing Interest

The authors declare that they have no known competing financial interests or personal relationships that could have appeared to influence the work reported in this paper.

References

[1] G. Konstantatos, E.H. Sargent, Nanostructured materials for photon detection, Nat. Nanotechnol. 5 (2010) 391–400, https://doi.org/10.1038/nnano.2010.78.
[2] G. Konstantatos, J. Clifford, L. Levina, E.H. Sargent, Sensitive solution-processed visible-wavelength photodetectors, Nat. Photonics 1 (9) (2007) 531–534, https://doi.org/10.1038/nphoton.2007.147.
[3] K.-J. Baeg, M. Binda, D. Natali, M. Caironi, Y.-Y. Noh, Organic light detectors: photodiodes and phototransistors, Adv. Mater. 25 (31) (2013) 4267–4295, https://doi.org/10.1002/adma.201204979.
[4] A.J.H. Gong, Xiong, Minghong Tong, Yangjun Xia, Wanzhu Cai, Ji Sun Moon, Yong Cao, Yu Gang, Chan-Long Shieh, Boo Nilsson, High-detectivity polymer photodetectors with spectral response from 300 nm to 1450 nm, Science (80-.) 325 (2014), https://doi.org/10.1126/science.1176706.
[5] R.D. Jansen-van Vuuren, A. Armin, A.K. Pandey, P.L. Burn, P. Meredith, Organic photodiodes: the future of full color detection and image sensing, Adv. Mater. 28 (2016) 4766–4802, https://doi.org/10.1002/adma.201505405.
[6] L.H. Zeng, S.H. Lin, Z.J. Li, Z.X. Zhang, T.F. Zhang, C. Xie, C.H. Mak, Y. Chai, S. P. Lau, L.B. Luo, Y.H. Tsang, Fast, self-driven, air-stable, and broadband photodetector based on vertically aligned PtSe2/GaAs heterojunction, Adv. Funct. Mater. 28 (2018) 1–11, https://doi.org/10.1002/adfm.201705970.
[7] D.i. Wu, Z. Zhao, W. Lu, L. Rogée, L. Zeng, P. Lin, Z. Shi, Y. Tian, X. Li, Y.H. Tsang, Highly sensitive solar-blind deep ultraviolet photodetector based on graphene/PtSe2/β-Ga2O3 2D/3D Schottky junction with ultrafast speed, Nano Res. 14 (6) (2021) 1973–1979, https://doi.org/10.1007/s12274-021-3346-7.
[8] L. Zeng, D. Wu, J. Jie, X. Ren, X. Hu, S.P. Lau, Y. Chai, Y.H. Tsang, Van der Waals epitaxial growth of mosaic-like 2D platinum ditelluride layers for room-temperature mid-infrared photodetection up to 10.6 μm, Adv. Mater. 32 (2020) 1–11, https://doi.org/10.1002/adma.202004412.
[9] D.i. Wu, J. Guo, C. Wang, X. Ren, Y. Chen, P. Lin, L. Zeng, Z. Shi, X.J. Li, C.-X. Shan, J. Jie, Ultrabroadband and high-detectivity photodetector based on WS2/Ge heterojunction through defect engineering and interface passivation, ACS Nano 15 (6) (2021) 10119–10129, https://doi.org/10.1021/acsnano.1c0200710.1021/acsnano.1c02007.s001.
[10] D.i. Wu, J. Guo, J. Du, C. Xia, L. Zeng, Y. Tian, Z. Shi, Y. Tian, X.J. Li, Y.H. Tsang, J. Jie, Highly polarization-sensitive, broadband, self-powered photodetector based on graphene/PdSe2/germanium heterojunction, ACS Nano 13 (9) (2019) 9907–9917, https://doi.org/10.1021/acsnano.9b0399410.1021/acsnano.9b03994.s001.
[11] L.H. Zeng, Q.M. Chen, Z.X. Zhang, D. Wu, H. Yuan, Y.Y. Li, W. Qarony, S.P. Lau, L. B. Luo, Y.H. Tsang, Multilayered PdSe2/perovskite schottky junction for fast, self-powered, polarization-sensitive, broadband photodetectors, and image sensor application, Adv. Sci. 6 (2019), https://doi.org/10.1002/advs.201901134.
[12] P. Xiao, J. Mao, K. Ding, W. Luo, W. Hu, X. Zhang, X. Zhang, J. Jie, Solution-processed 3D RGO–MoS2/pyramid Si heterojunction for ultrahigh detectivity and ultra-broadband photodetection, Adv. Mater. 30 (2018) 1–11, https://doi.org/10.1002/adma.201801729.
[13] L.H. Zeng, D. Wu, S.H. Lin, C. Xie, H.Y. Yuan, W. Lu, S.P. Lau, Y. Chai, L.B. Luo, Z. J. Li, Y.H. Tsang, Controlled synthesis of 2D palladium diselenide for sensitive photodetector applications, Adv. Funct. Mater. 29 (2019) 1–9, https://doi.org/10.1002/adfm.201806878.
[14] R. Ahmed, M.C. Gupta, Mid-infrared photoresponse of electrodeposited PbSe thin films by laser processing and sensitization, Opt. Lasers Eng. 134 (2020) 106299, https://doi.org/10.1016/j.optlaseng.2020.106299.
[15] R.A. Ismail, S.S. Shaker, A.M. Mousa, Study the optoelectronic properties of PbI 2 nanorods / Si photodetector prepared by magnetic field-assisted laser deposition route, Opt. Laser Technol. 140 (2021) 107042, https://doi.org/10.1016/j.optlastec.2021.107042.
[16] Z.G. Bafghi, N. Manavizadeh, Low power ZnO nanorod-based ultraviolet photodetector: effect of alcoholic growth precursor, Opt. Laser Technol. 129 (2020), https://doi.org/10.1016/j.optlastec.2020.106310.
[17] R. Lukac, Single-sensor imaging in consumer digital cameras: a survey of recent advances and future directions, J. Real-Time Image Process. 1 (2006) 45–52, https://doi.org/10.1007/s11554-006-0003-z.
[18] H. Park, Y. Dan, K. Seo, Y.J. Yu, P.K. Duane, M. Wober, K.B. Crozier, Filter-free image sensor pixels comprising silicon nanowires with selective color absorption, Nano Lett. 14 (4) (2014) 1804–1809, https://doi.org/10.1021/nl404379w.

[19] T. Xu, Y.K. Wu, X. Luo, L.J. Guo, Plasmonic nanoresonators for high-resolution colour filtering and spectral imaging, Nat. Commun. 1 (2010) 59, https://doi.org/10.1038/ncomms1058.
[20] S.J. Lim, D.S. Leem, K.B. Park, K.S. Kim, S. Sul, K. Na, G.H. Lee, C.J. Heo, K.H. Lee, X. Bulliard, R.I. Satoh, T. Yagi, T. Ro, D. Im, J. Jung, M. Lee, T.Y. Lee, M.G. Han, Y. W. Jin, S. Lee, Organic-on-silicon complementary metal-oxide-semiconductor colour image sensors, Sci. Rep. 5 (2015) 1–7, https://doi.org/10.1038/srep07708.
[21] Q. Lin, A. Armin, P.L. Burn, P. Meredith, Filterless narrowband visible photodetectors, Nat. Photonics 9 (10) (2015) 687–694, https://doi.org/10.1038/nphoton.2015.175.
[22] A. Armin, R.D. Jansen-Van Vuuren, N. Kopidakis, P.L. Burn, P. Meredith, Narrowband light detection via internal quantum efficiency manipulation of organic photodiodes, Nat. Commun. 6 (2015), https://doi.org/10.1038/ncomms7343.
[23] S.K. Chamoli, G. Verma, S.C. Singh, Phase change material-based nano-cavity as an efficient optical modulator, Nanotechnology. 32 (2021) 095207.
[24] S.K. Chamoli, G. Verma, S.C. Singh, C. Guo, Phase change material based hot electron photodetection, Nanoscale 13 (2) (2021) 1311–1317.
[25] M. Wuttig, S. Raoux, The science and technology of phase change materials, Zeitschrift Fur Anorg, Und Allg Chemie. 638 (15) (2012) 2455–2465, https://doi.org/10.1002/zaac.201200448.
[26] P. Noé, C. Vallée, F. Hippert, F. Fillot, J.-Y. Raty, Phase change materials for non-volatile memory devices: from technological challenges to materials science issues, Semicond. Sci. Technol. 33 (1) (2018) 013002, https://doi.org/10.1088/1361-6641/aa7c25.
[27] R. Kondrotas, C. Chen, J. Tang, Sb2S3 solar cells, Joule 2 (5) (2018) 857–878, https://doi.org/10.1016/j.joule.2018.04.003.
[28] R.R. Prabhakar, T. Moehl, S. Siol, J. Suh, S.D. Tilley, Sb2S3/TiO2heterojunction photocathodes: band alignment and water splitting properties, Chem. Mater. 32 (2020) 7247–7253, https://doi.org/10.1021/acs.chemmater.0c01581.
[29] S. Chen, X. Qiao, F. Wang, Q. Luo, X. Zhang, X. Wan, Y. Xu, X. Fan, Facile synthesis of hybrid nanorods with the Sb2Se3/AgSbSe2 heterojunction structure for high performance photodetectors, Nanoscale 8 (4) (2016) 2277–2283.
[30] M. Zhong, X. Wang, S. Liu, B. Li, L. Huang, Y. Cui, J. Li, Z. Wei, High-performance photodetectors based on Sb2S3 nanowires: wavelength dependence and wide temperature range utilization, Nanoscale 9 (2017) 12364–12371, https://doi.org/10.1039/c7nr03574h.
[31] A. Bera, A. Das Mahapatra, S. Mondal, D. Basak, Sb2S3/Spiro-OMeTAD inorganic-organic hybrid p-n junction diode for high performance self-powered photodetector, ACS Appl. Mater. Interfaces 8 (50) (2016) 34506–34512, https://doi.org/10.1021/acsami.6b0994310.1021/acsami.6b09943.s001.
[32] C.L. Hassam, F. Sciortino, N.T.K. Nguyen, B. Srinivasan, K. Ariga, F. Gascoin, F. Grasset, T. Mori, T. Uchikoshi, Y. Thimont, D. Berthebaud, Robust, transparent hybrid thin films of phase-change material Sb2S3prepared by electrophoretic deposition, ACS Appl. Energy Mater. 4 (9) (2021) 9891–9901, https://doi.org/10.1021/acsaem.1c0189910.1021/acsaem.1c01899.s001.
[33] K. Zhang, T. Luo, H. Chen, Z. Lou, G. Shen, Au-nanoparticles-decorated Sb2S3 nanowire-based flexible ultraviolet/visible photodetectors, J. Mater. Chem. C 5 (13) (2017) 3330–3335.
[34] V. Srivastava, P. Mishra, Sunny, CMOS compatible novel integration solution for broad range tunable photodetection using phase-change material based heterostructures, Sci. Rep. 10 (2020) 1–14, https://doi.org/10.1038/s41598-020-67950-2.
[35] S. Abdollahramezani, O. Hemmatyar, H. Taghinejad, A. Krasnok, Y. Kiarashinejad, M. Zandehshahvar, A. Alù, A. Adibi, Tunable nanophotonics enabled by chalcogenide phase-change materials, Nanophotonics 9 (5) (2020) 1189–1241, https://doi.org/10.1515/nanoph-2020-0039.
[36] M. Wuttig, H. Bhaskaran, T. Taubner, Phase-change materials for non-volatile photonic applications, Nat. Photonics 11 (8) (2017) 465–476, https://doi.org/10.1038/nphoton.2017.126.
[37] W. Dong, H. Liu, J.K. Behera, L. Lu, R.J.H. Ng, K.V. Sreekanth, X. Zhou, J.K. W. Yang, R.E. Simpson, Wide bandgap phase change material tuned visible photonics, Adv. Funct. Mater. 29 (2019) 1–9, https://doi.org/10.1002/adfm.201806181.
[38] Y. Au, H. Bhaskaran, C.D. Wright, Phase-change devices for simultaneous optical-electrical applications, Sci. Rep. (2017) 1–7, https://doi.org/10.1038/s41598-017-10425-8.
[39] C. Rios, Y. Zhang, S. Deckoff-Jones, H. Li, J.B. Chou, H. Wang, M. Shalaginov, C. Roberts, C. Gonaalves, V. Liberman, T. Gu, J. Kong, K. Richardson, J. Hu, Reversible switching of optical phase change materials using graphene microheaters, in: 2019 Conf. Lasers Electro-Optics, CLEO 2019 – Proc., 2019, pp. 10–11. https://doi.org/10.23919/CLEO.2019.8749567.
[40] S. Chamoli, M. Elkabbash, J. Zhang, Dynamic control of spontaneous emission rate using tunable hyperbolic metamaterials, Opt. Lett. 45 (2020), https://doi.org/10.1364/OL.385844.
[41] X. Wang, K. Ehrhardt, C. Tallet, M. Warenghem, A. Baron, A. Aradian, M. Kildemo, V. Ponsinet, [INVITED] Hyperbolic-by-design self-assembled metamaterial based on block copolymers lamellar phases $, Opt. Laser Technol. 88 (2017) 85–95, https://doi.org/10.1016/j.optlastec.2016.08.005.
[42] L. Shengyong, A. Xiaochuan, W. Ronghua, C. Jiajun, J. Tao, Enhancement of multi-band absorption based on compound structure metamaterials, Opt. Laser Technol. 115 (2019) 239–245, https://doi.org/10.1016/j.optlastec.2019.02.026.
[43] C. Ghosh, B.P. Varma, Optical properties of amorphous and crystalline Sb2S3 thin films, Thin Solid Films 60 (1) (1979) 61–65, https://doi.org/10.1016/0040-6090(79)90347-X.
[44] P. Peumans, A. Yakimov, S.R. Forrest, Small molecular weight organic thin-film photodetectors and solar cells, J. Appl. Phys. 93 (7) (2003) 3693–3723, https://doi.org/10.1063/1.1534621.
[45] Y. Jia, H. Deng, X. Lin, S. Chen, Y. Xia, Z. Wu, J. Yu, S. Cheng, Y. Lai, Depleted Sb2S3 thin film photoconductive detectors with fast response speed and high polarization sensitivity, Adv. Mater. Interfaces 2101504 (2021) 1–8, https://doi.org/10.1002/admi.202101504.
[46] A.P. Raman, M.A. Anoma, L. Zhu, E. Rephaeli, S. Fan, Passive radiative cooling below ambient air temperature under direct sunlight, Nature 515 (7528) (2014) 540–544, https://doi.org/10.1038/nature13883.
[47] K. Wang, G. Luo, X. Guo, S. Li, Z. Liu, C. Yang, Radiative cooling of commercial silicon solar cells using a pyramid-textured PDMS film, Sol. Energy 225 (2021) 245–251, https://doi.org/10.1016/j.solener.2021.07.025.
[48] K. Te Lin, J. Han, K. Li, C. Guo, H. Lin, B. Jia, Radiative cooling: fundamental physics, atmospheric influences, materials and structural engineering, applications and beyond, Nano Energy 80 (2021), https://doi.org/10.1016/j.nanoen.2020.105517.
[49] L. Zhu, A. Raman, K.X. Wang, M.A. Anoma, S. Fan, Radiative cooling of solar cells, Optica. 1 (2014) 32, https://doi.org/10.1364/optica.1.000032.